DEPARTMENT OF ELECTRICAL AND COMPUTER ENGINEERING
DUKE UNIVERSITY

Monte Carlo Simulation of Charge Transport in Organic Solar Cells

Undergraduate Thesis

Xin Xu
Advisor: Associate Professor Adrienne D. Stiff-Roberts
4/18/2012

Contents

Abstract

Organic solar cells have advantages over the traditional inorganic solar cells. The flexibility and light-weight of an organic solar device lead to novel deployment unattainable by inorganic solar devices. There is a wide range of materials that can be used to fabricate an organic solar cell with many suitable conducting polymers and small molecules. The large number of appropriate materials means that it is possible to tune an organic cell to target specific wavelengths of light by targeting specific band gaps. Despite all these benefits, the commercialization of organic solar devices has been limited by their low efficiency. One path to raising the efficiency is to better understand how the morphology or internal structure of the solar cell influences charge transport. The work presented here is a Dynamical Monte Carlo (DMC) simulation that can model the processes that govern the conversion of light to electrical power. The Monte Carlo simulation describes how the interacting particles in the solar cell move and behave. This simulation can provide insight to how the structure of the cell can influence both charge creation and charge collection. The DMC simulations were performed for two archetypal organic solar cell material systems: CuPc-C60 and P3HT-PCBM. Various morphologies were used for these material systems to examine the effect of morphology on both internal and external quantum efficiency.

Introduction

Since the introduction of the bilayer donor-acceptor heterojunction organic solar cell by C.W. Tang in 1986 [1], organic solar cell efficiencies have been rising. However, the efficiencies of organic photovoltaic (OPV) cells still lag behind their inorganic counterparts, with the most efficient OPV cell rated at 10% efficiency [2]. The challenges to successful organic solar cell design are numerous. Chief among these is that organic solar cell physics differs greatly from that of inorganic solar cells. Thus, the theoretical framework developed to describe inorganic solar cells cannot be directly applied to organics. A new approach for organic solar cells is needed.

The Organic Solar Cell

The physics and analysis of organic solar cells differ greatly from their inorganic counterparts. The energy states are distributed differently in an organic vs. inorganic solar cell. For an inorganic solar cell, the periodicity of the inorganic semiconductor crystal lattice leads to the formation of conduction bands and valence bands. The charges move along these bands and carrier movement can be solved analytically with Bloch wave functions [3]. Organic solar cells have two important energy states: highest occupied molecular orbital (HOMO) and lowest unoccupied

molecular orbital (LUMO). Rather than form energy bands, the disorder of the organic cell leads to highly localized states. Charge movement is described by hopping from localized state to localized state [3]. Figure 1(a) and (b) show the movement of charges in the energy structure of an inorganic semiconductor and an organic semiconductor, respectively. The hopping behavior of charge movement in the organic semiconductor lends itself well to be described by the Dynamic Monte Carlo method.

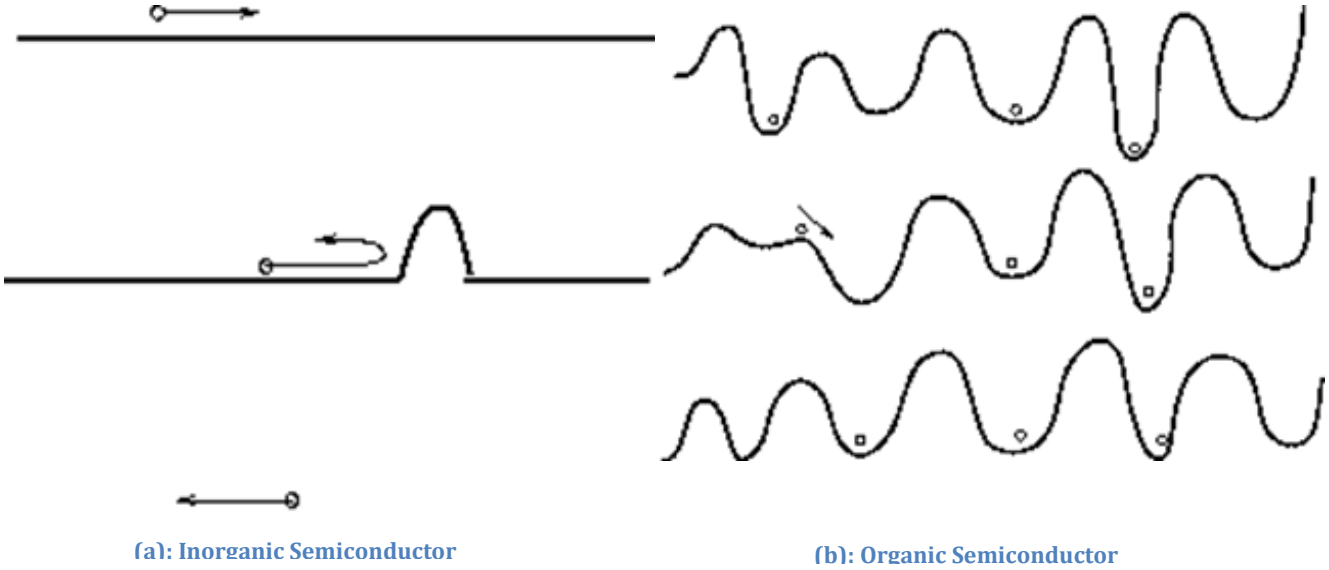

(a): Inorganic Semiconductor (b): Organic Semiconductor

Figure 1: Charges moving through the energy structure of an inorganic semiconductor and an organic semiconductor [23]

The basic organic solar cell is a stacked structure. Starting from the bottom, there is the glass substrate, the indium tin oxide (ITO) layer, the PEDOT-PSS layer, the active layer, and lastly the aluminum top contact. An example of this structure can be seen in Figure 2. The ITO is a transparent layer which serves as the hole contact. The PEDOT-PSS layer is a hole transporting layer, which matches well energetically with the ITO contact, serves to smooth the rough ITO layer for better active layer deposition, and blocks electrons to prevent recombination at the electrode. The active region layer is where absorbed photons are converted into holes and electrons and consists of two types of materials, an electron conducting material and a hole conducting material. Hereafter, the electron and hole conducting materials will be referred to as the acceptor and donor materials, respectively. For this work, three different active region morphologies are considered: the bilayer which is a layer of acceptor material on top of a layer of donor material, the chessboard which is a morphology with alternating columns of acceptor and donor materials, and the bulk heterojunction (BHJ) which is a mixture of acceptor and donor material. Lastly, the aluminum layer is the electron contact.

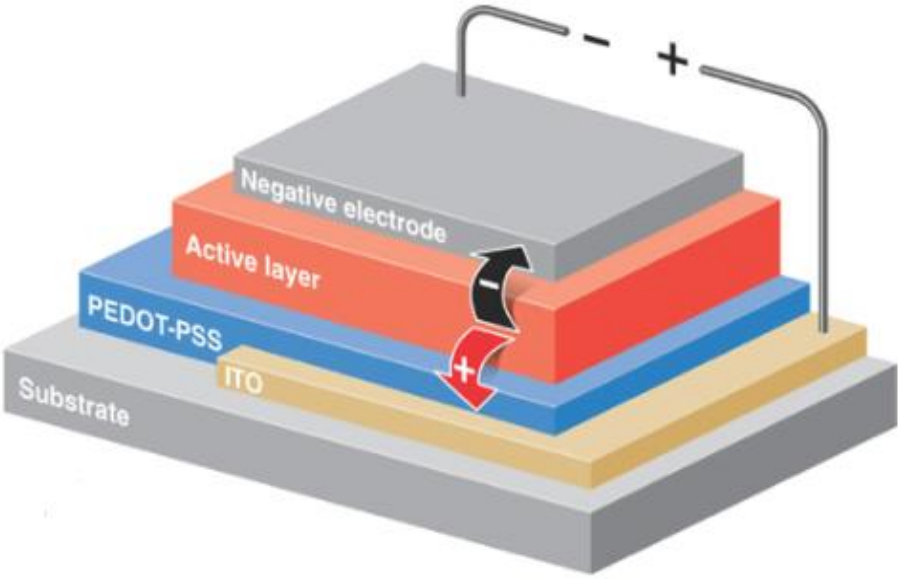

Figure 2: The structure of the organic solar cell. Figure from [24].

Photovoltaic Process

The photovoltaic process starts with the absorption of a photon in the active region layer which generates an exciton. The exciton is a quasiparticle representing a tightly bound electron and hole pair. This exciton diffuses through the cell until it reaches a donor-acceptor material interface where it dissociates into the electron and hole. The exciton can also recombine before it reaches an interface. An exciton that recombines does not contribute to the photovoltaic effect. The generated electron and hole will only travel in the acceptor and donor material respectively. These charge carriers move through their respective material type until they reach a contact, from which they can provide power to an external circuit. A diagram of this process can be seen in Figure 3.

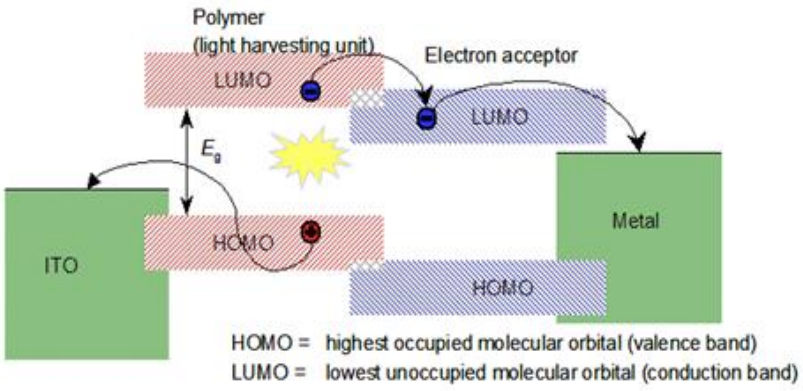

Figure 3: The photovoltaic process in an organic solar cell. Figure from [25]

Two figures of merit for the organic solar cell is the external quantum efficiency (EQE), denoted as η_{EQE}, and the internal quantum efficiency (IQE) denoted as η_{IQE}. The EQE is the number of carriers collected at the contacts of the solar cell divided by the number of incident photons. To determine the EQE, the efficiencies of four processes need to be considered: the absorption efficiency describing the number of excitons generated for a given number of incident photons, the exciton diffusion efficiency describing the number of excitons that reach a donor-acceptor interface without recombination, the charge transfer efficiency describing the number of dissociated electrons and holes generated for a given number of excitons that reach a donor-acceptor interface, and the charge collection efficiency describing the number of charges collected at the contact for a given number of dissociated electrons and holes. The calculation of EQE is as follows:

$$\eta_{EQE} = \eta_{\alpha}\eta_{IQE} = \eta_{\alpha}\eta_{ED}\eta_{CT}\eta_{CC} \quad (1)$$

where η_{α} is the absorption efficiency, η_{ED} is the exciton diffusion efficiency, η_{CT} is the charge transfer efficiency, and η_{CC} is the charge collection efficiency. Generally $\eta_{CT} = 1$ for organic donor-acceptor solar cells due to the speed of the process (~10-100 fs) so the EQE and the IQE are only functions of η_{α}, η_{ED}, and η_{CC} [4].

Literature Review

Watkins *et al.* first demonstrated the usage of a Dynamical Monte Carlo (DMC) model to simulate charge transport in an organic solar cell [5]. They modeled a polymer blend of PFB and F8BT, and obtained a peak IQE that exceeds 50% for a bulk heterojunction, which is of the right order compared to experimental measurements. Watkins also described a method to generate the bulk heterojunction morphologies with varying domain sizes. Details on this method will be discussed in the Model Description section. The focus of Watkins' work was on testing the validity of this type of simulation and to find general trends rather than to predict the exact IQE for a device. As such, he made three key simplifications: the mobility of holes and electrons are the same, there is no energy disorder for the localized hopping states, and the exciton generation rate was determined by an order of magnitude calculation and assumed to follow a Gaussian distribution with respect to the thickness of the solar cell.

After Watkins demonstrated the potential of the DMC method, Fan Yang and Stephen Forrest used it to simulate the archetypal small molecule organic system of CuPc and C60 [6]. In addition, they corrected the simplifying assumptions that Watkins had made. The equations and Dynamical Monte Carlo method are equally applicable to the new material system. Yang and Forrest allowed the mobility for holes and electrons to be different, introduced a Gaussian energy

disorder for the localized states, and calculated the exciton generation rate by multiplying the optical field intensity within the cell and with the material absorption coefficient of the cell. By improving the accuracy of these components of the model, Yang and Forrest obtained simulated EQEs very close to experimental measurements. For the bilayer morphology, the simulated EQE is 0.13 compared to a measured EQE of 0.14±0.1, and for the bulk heterojunction morphology the simulated EQE is 0.16 compared to a measured EQE of 0.16±0.1.

Motivation

The motivation for this work comes from the Stiff-Roberts Lab's need for an in house simulation tool for organic solar cells. As opposed to the Yang and Forrest model for small molecule solar cells of CuPc and C60, we are more focused on the bulk heterojunction solar cell comprising of PCBM small molecules embedded in a P3HT polymer matrix. Additionally, we use a unique deposition technique called matrix assisted pulsed laser evaporation (MAPLE) to build solar cells. MAPLE gives more control of the morphology of the solar cell than other deposition techniques like drop-casting or spin-casing. We wish to have a tool to model these morphologies. By building a model more suited to our unique needs, we can save time, materials and costs by predicting the performance of our solar cells before we build them.

Model Description

The model that was built as part of this thesis work consisted of three parts: a Metropolis Algorithm Monte Carlo for the Ising Model to generate the bulk heterojunction morphologies, a transfer matrix calculation from which an exciton generation rate and distribution is determined, and a Dynamical Monte Carlo to simulate charge transport within the organic solar cell.

Bulk Heterojunction Morphology Generator

The first part of the model is the generation of the random bulk heterojunction (BHJ) morphology. This is the same method as used by Watkins *et al* [5]. These BHJ morphologies were generated using the Ising Model and Kawasaki spin dynamics governed by the Metropolis Algorithm Monte Carlo. The method starts by assigning every lattice point or occupation site in our organic solar cell a "spin" of "1" or "-1", which corresponds to either a donor material or an acceptor material. Our initial morphology is thus a completely disordered random state.

The Metropolis algorithm is primarily used to simulate how systems in an excited state relax towards equilibrium. In the case of our morphology generation, as the energy of the system lowers and heads towards "equilibrium", larger grain sizes will form and the disorder of the system will be lowered. To use the Metropolis algorithm, we need a measure of the energy of the system. We assign each lattice site an energy according to the Ising Hamiltonian shown in Equation 2 which will give the energy of site *i*.

$$\epsilon_i = -\frac{1}{2}\sum_j (\delta_{s_i,s_j} - 1) \tag{2}$$

In Equation 2, δ_{s_i,s_j} is the Kronecker delta where s_i and s_j are the spins of site *i* and *j*. The summation over *j* corresponds to the first and second nearest neighbors to site *i*. The energy contribution of second nearest neighbors is weighed by a factor of $\frac{1}{\sqrt{2}}$.

To lower the energy of the system, we randomly pick two neighboring pairs of sites and attempt to swap their spins. The energy change of the system, denoted as $\Delta\epsilon$, caused by this swap determines the probability of whether or not the swap is accepted. The probability is calculated using Equation 3 where T is in units of $1/k_B$. As the simulation runs, the energy of the system will decrease leading to the formation of larger and larger grains of material.

$$P(\Delta\epsilon) = \frac{e^{-\Delta\epsilon/(k_B T)}}{1 + e^{-\Delta\epsilon/(k_B T)}} \tag{3}$$

One way of controlling the morphologies generated by this simulation is by changing the runtime of the simulation. The Monte Carlo step is the unit of measurement for the simulation runtime. One Monte Carlo step is defined as the number of swap attempts that equal the total number of lattice sites in the system. Both Watkins and Yang controlled the morphology by running the simulation for differing number of Monte Carlo steps. However, interesting morphologies can be generated by varying the input temperature to the simulation. Neither Watkins nor Yang used temperature to control morphology. For example, running 100 MC steps at T = 1 and then 100 MC steps at T = 10, and then 100 MC steps at T = 1 leads to a different morphology than 300 MC steps at T = 1. By running the simulation at higher temperatures, it is possible to escape an energy-well and relax into another lower energy state for the system. Some work is done to observe how the morphology changes as a function of temperature and the results of this are presented.

The morphology generator tool is built using C. The morphology pictures are generated using MATLAB. Morphologies took anywhere from ten minutes to two hours to generate.

Exciton Generation Rate

The method to determine the exciton generation rate is the same as the method described by Yang and Forrest [6]. The optical field intensity which is a function of wavelength from 300 nm to 900 nm and distance from the reflective cathode is calculated by treating the solar cell as a lossy microcavity. The interfaces between the layers of the solar cell are assumed to be optically flat and the materials are assumed to be isotropic with complex indices of refraction [4]. The optical field is determined using the transfer matrix method which uses Equations 4 through 26 [4] [7].

The tangential component of electrical field must be continuous at each interface and this boundary condition can be described using 2x2 matrices. The propagation of the incident solar E-field through the solar cell can be solved using these 2x2 matrices. To calculate the E-field within the solar cell, we assume the solar cell multilayer of ITO, PEDOT-PSS, active layer, and aluminum is sandwiched between two semi-infinite layers: the glass substrate and air. This geometry can be seen in Figure 4. The incident solar E-field is along the surface normal coming from left of the substrate and heading right towards the substrate and has magnitude derived from the AM1.5 G solar spectrum.

The calculations for optical field intensity presented here differed from those done by Yang and Forrest by the inclusion of a 30 nm thick PEDOT-PSS layer. The PEDOT-PSS layer will be deposited in future devices and its inclusion is needed to align the simulation device design with real device design. Furthermore, it was unclear what thicknesses were assumed by Yang and Forrest for the ITO and aluminum contact layers so typical thicknesses of 100 nm were used.

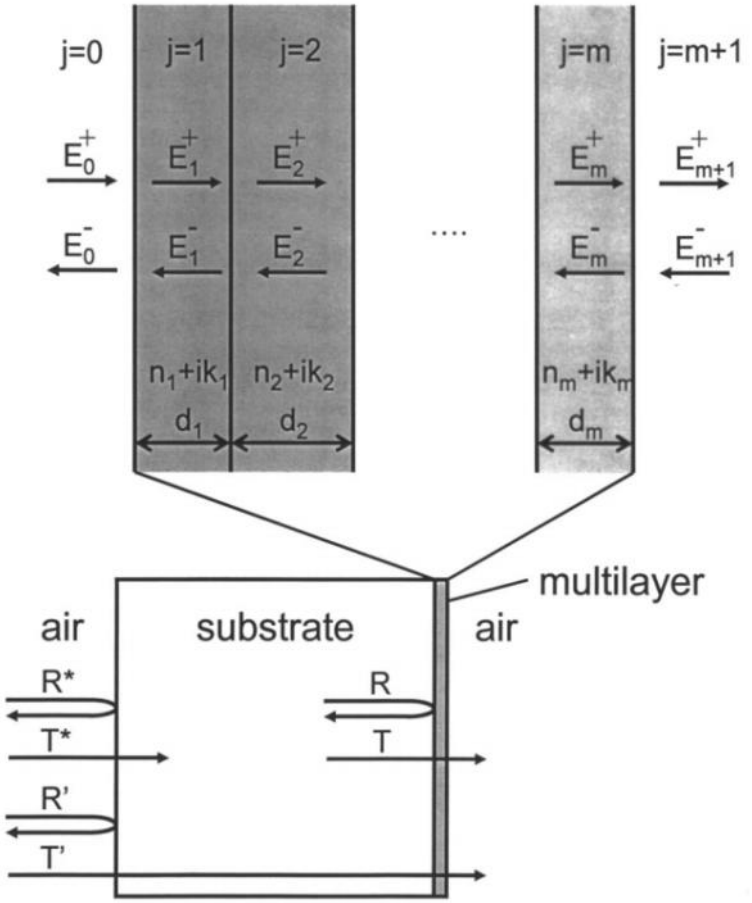

Figure 4: Geometry used for the optical electrical field calculation. Layer 0 and m+1 are the glass substrate and air respectively.

At an interface between layer j and k, the propagation of the electric field is described by the interface matrix I_{jk}, and as seen in Equation 4. The terms r_{jk} and t_{jk} that make up the interface matrix are the complex valued Fresnel coefficients, where n_j and n_k are the complex indices of refraction for layer j and k respectively.

$$\begin{bmatrix} E_j^+ \\ E_j^- \end{bmatrix} = I_{jk} \begin{bmatrix} E_k^+ \\ E_k^- \end{bmatrix} = \begin{bmatrix} \frac{1}{t_{jk}} & \frac{r_{jk}}{t_{jk}} \\ \frac{r_{jk}}{t_{jk}} & \frac{1}{t_{jk}} \end{bmatrix} \begin{bmatrix} E_k^+ \\ E_k^- \end{bmatrix} \tag{4}$$

$$r_{jk} = (n_j - n_k)/(n_j + n_k) \tag{5}$$

$$t_{jk} = 2n_j/(n_j + n_k) \tag{6}$$

There is the propagation matrix L_j which describes the absorption and phase shift of the E-field within layer *j*. Here n_j is the complex index of refraction of layer *j* and λ is the wavelength in vacuum.

$$L_j = \begin{bmatrix} e^{-i\xi_j d_j} & 0 \\ 0 & e^{i\xi_j d_j} \end{bmatrix} \tag{7}$$

$$\xi_j = \left(\frac{2\pi}{\lambda}\right) n_j \tag{8}$$

The total transfer matrix S describes how the E-field propagates through our stacked geometry and is a multiplication of all of the interface matrices and propagation matrices from one side of the stack to the other side.

$$\begin{bmatrix} E_0^+ \\ E_0^- \end{bmatrix} = S \begin{bmatrix} E_{m+1}^+ \\ E_{m+1}^- \end{bmatrix} \tag{9}$$

$$S = \begin{bmatrix} S_{11} & S_{12} \\ S_{21} & S_{22} \end{bmatrix} = \left(\prod_{n=1}^{m} I_{(n-1)n} \, L_n \right) I_{m(m+1)} \tag{10}$$

The total transmission and reflection coefficients for the whole multilayer can be calculated using Equation11 and 12. The transmittance and reflectance of the multilayer is determined using Equations 13 and 14.

$$r = E_0^- / E_0^+ = S_{21} / S_{11} \tag{11}$$

$$t = E_{m+1}^+ / E_0^+ = S_{11}^{-1} \tag{12}$$

$$T = |t|^2 n_{m+1} / n_0 \tag{13}$$

$$R = |r|^2 \tag{14}$$

The transmittance and reflectance determined in Equations 13 and 14 are for the multilayer, but it does not take into account the glass substrate. Rather than describe the glass substrate with a transfer matrix, the transmittance and reflectance are corrected to account for the incident light transmitting through the glass substrate. The corrected transmittance and reflectance are denoted as R' and T' respectively.

$$R' = \frac{R^* + R - 2R^* R}{1 - R^* R} \tag{15}$$

$$T' = \frac{T^* T}{1 - R^* R} \tag{16}$$

$$R^* = \left|\frac{1 - n_0}{1 + n_0}\right|^2 \tag{17}$$

$$T^* = n_0 \left|\frac{2}{1 + n_0}\right|^2 \tag{18}$$

The absorption efficiency of the cell is shown in Equation 19.

$$\eta_\alpha = 1 - R' - T' \tag{19}$$

Since this absorption efficiency is wavelength dependent, a total absorption for the system is needed. This is calculated by using a weighted average of the efficiencies at each wavelength. The weight is determined by the power at that wavelength compared to the total power for all wavelengths from 300 to 900 nm.

To calculate the exciton generation rate, the electric field through each layer needs to be known. From the electric field, the optical field intensity can be calculated. The first step to find the electric field through an arbitrary layer *j*, is to split the total transfer matrix *S* into three separate matrices.

$$S = S_j^- L_j S_j^+ \tag{20}$$

$$S_j^- = \left(\prod_{n=1}^{j-1} I_{(n-1)n} L_n\right) I_{(j-1)j} \tag{21}$$

$$S_j^+ = \left(\prod_{n=j+1}^{m} I_{(n-1)n} L_n\right) I_{m(m+1)} \tag{22}$$

The relationship between the electric field propagating in the positive direction in layer *j* and the incident electric field is shown in Equation 23 and the relationship for the negatively propagating electric field is shown in Equation 24.

$$\frac{E_j^+}{E_0^+} = t_j^+ = \frac{\frac{1}{S_{j11}^-}}{1 + \frac{S_{j12}^- S_{j21}^+}{S_{j11}^- S_{j11}^+} e^{i2\xi_j d_j}} \tag{23}$$

$$\frac{E_j^-}{E_0^+} = t_j^- = t_j^+ \frac{S_{j21}^+}{S_{j11}^+} e^{i2\xi_j d_j} \tag{24}$$

The total electric field within layer j is then given by Equation 25, where x is an arbitrary position inside layer *j,* and E_0^+ is the electric field of the incident positively propagating wave. x is set to be zero at the reflecting cathode.

$$E_j(x) = E_j^+(x) + E_j^-(x) = (t_j^+ e^{i\xi_j x} + t_j^- e^{-i\xi_j x})E_0^+ \tag{25}$$

Converting from total electric field to optical field intensity is a simple matter of applying Equation 26, where c is the speed of light, n is the real component for the index of refraction of layer j, and ϵ_0 is the vacuum permittivity. This intensity is for a single wavelength, as the indices of refraction for the layers in the multilayer are wavelength dependent.

$$I_j(x) = \frac{cn\epsilon_0}{2}\left|E_j(x)\right|^2 \tag{26}$$

To get the exciton generation rate within layer j as a function of both wavelength and position, we multiply the optical field intensity from Equation 26 with the absorption coefficient from Equation 27. In equation 27, k is the imaginary component of the index of refraction for layer j and λ is the wavelength in vacuum.

$$\alpha = \frac{4\pi k}{\lambda} \tag{27}$$

The wavelength dependence of the exciton generation rate is removed by integrating over the set of wavelengths from 300 nm to 900 nm. Then to calculate the total exciton generation rate, the generation rate is integrated over the thickness of the cell to get rid of the position dependence. Excitons will appear in our solar cell at the total exciton generation rate. Excitons will be located randomly along the cross-sectional area of the solar cell, but will be generated along the thickness according to the exciton distribution. The exciton distribution is proportional to the position dependent exciton generation rate.

The transfer matrix method calculations were computed in Matlab. The indices of refraction for the calculations were taken from various sources. The indices of refraction for CuPc, C60 and the 1:1 blend of CuPc:C60 were from Datta *et al* [8]. The indices of refraction for P3HT:PCBM blends were taken from Monestier *et al* [9]. The indices of refraction for glass and PEDOT-PSS were taken from Hoppe *et al* [10]. Lastly the indices of refraction for ITO and aluminum were from the Refractive Index Database [11].

Charge Transport Model

The last part of the model is the Dynamical Monte Carlo (DMC) simulation used to track charge transport within an organic solar cell. Excitons, holes, and electrons are tracked through a cubic lattice of dimensions 100 x 100 x 60. The lattice constant a of the system determines the size of each lattice position. Excitons are continuously generated through the cell according to the exciton generation rate. Carriers are collected at the contacts, which are located at z = 0 and z = 60. The energy disorder is simulated by setting each lattice position to have a random energy distributed as a Gaussian [12]. The energy of each lattice position is then modified by the work function difference of the contacts which is 0.5 eV for aluminum-ITO [5]. Further modifying the energy at a lattice point is the presence of Coulombic interactions for charge carriers. Coulomb interaction is evaluated up to six lattice points away, which given a lattice constant of 1 nm, means 6 nm. This is larger than the Debye length (4 nm) typical of organic materials [6].

We used the DMC algorithm known as the First Reaction Method (FRM) for our simulation. In FRM, the probabilities of the possible actions are generated for a particle once that particle has executed a previous action. In comparison, the full DMC recalculates the actions of every particle whenever any particle executes an action. The FRM reduces computation significantly compared to the full DMC, and it has been shown that FRM and full DMC differ by less than 0.5% for organic systems because the low density of particles within the cell makes interactions rare [6].

The FRM algorithm uses a queue of events sorted by their time, and the event with the shortest time is at the front of the queue. The simulation starts by removing the first event from the queue and executing it. The time of all events still in the queue is updated by subtracting the time of the executed event from the time of every event still in the queue. After the event is executed, the state of the system will change and new possible events are added to the queue.

To fill the queue with events, each particle will generate a list of possible events that it can undertake. The event with the shortest time will be the action that the particle takes and this event and its associated time is added to the queue. The particle will wait until this event is executed, at which point it will generate a new set of events to pick from and place in the queue.

An exciton can move, dissociate, or recombine. Exciton movement is modeled by Förster energy transfer and can be seen in Equation 29. Equation 29 [5] [6] is the time for an exciton to move from position *i* to position *j*, where R_{ij} is the distance between *i* and *j*, R_0 is the exciton localization radius, τ_{ex} is the exciton lifetime, ΔE_{ij} is the energy difference between position *i* and *j*, and X is a random uniform distribution from 0 to 1. The exciton localization radius R_0 is calculated

by assuming that the exciton generally travels one lattice constant when it moves. A particle on a random walk will travel the square root of the number of hops multiplied by the distance of each hop. An exciton will travel its diffusion length over its lifetime, so by calculating how much time each hop takes and knowing both the exciton diffusion length and the lifetime, the exciton localization radius can be determined. The $\ln(X)$ in Equation 29 is used to add a degree of randomness to the exciton movement. The function $f(\Delta E_{ij})$ within Equation 29 and shown in Equation 28 serves to make the exciton more likely to travel from high energy to low energy. The other possible exciton actions are dissociation and recombination. Dissociation time is set to infinity when the exciton is not at an interface and zero when the exciton is at an interface. Recombination time is set to infinity until the exciton has been in the system for longer than its lifetime, at which point it is set to zero.

$$f(\Delta E_{ij}) = \begin{cases} e^{-\Delta E_{ij}/(k_B T)} & : \Delta E_{ij} > 0 \\ 1 & : \Delta E_{ij} < 0 \end{cases} \tag{28}$$

$$\tau_{eh} = -\tau_{ex} \left(\frac{R_{ij}}{R_0}\right)^6 \frac{\ln(X)}{f(\Delta E_{ij})} \tag{29}$$

A charge carrier can move, recombine, or be collected. Charge carrier movement is governed by Miller-Abrahams hopping [13] and can be seen in Equation 30 [5] [6]. Here, a is the lattice constant and γ is the charge localization constant which is 2 nm^{-1} for both material systems. For recombination events, the time is set to be infinity unless two opposite charge carriers are next to each other at which point it is given by Equation 31, where w_{recomb} is the recombination rate. Charge collection time is set to be infinity when the carrier is not next to a contact, but zero when it is.

$$\tau_{ch} = \frac{-qa^2}{6k_B T \mu_{n,p}} e^{2\gamma(R_{ij}-a)} \frac{\ln(X)}{f(\Delta E_{ij})} \tag{30}$$

$$\tau_{recomb} = -\frac{1}{w_{recomb}} \ln(X) \tag{31}$$

There is one final possible event which is not associated with a particle. It is the exciton generation event. The exciton generation event time is taken from the exciton generation rate calculated in the first part of the model. This time is multiplied by $\ln(X)$ like the other times to put a degree of randomness to the generation rate.

The equations presented here for the DMC simulation are very similar to those by Yang and Forrest [6]. However, they are not exactly the same. Several of the equations presented by Yang

and Forrest did not make numerical sense and some were not self-consistent. These were corrected and the reasons behind the corrections are in the Discussion section. Also there are many edge cases present in the simulation that were not discussed by Yang and Forrest or Watkins *et al.* Examples include: what happens if an exciton is to be generated in an occupied location; what happens if the hole has a recombination event with a neighboring electron, but the electron moves away before the recombination event executes; what to do if the lattice positions where a hole and electron are to be placed are occupied for an exciton dissociation event; etc.

The charge transport model used two sets of parameters depending on the material system. The parameters for CuPc and C60 material system are in Table 1. The parameters for P3HT and PCBM are shown in Table 2.

Table 1: Parameters for the CuPc and C60 blended films [6]

Property	CuPc	C60
Relative dielectric constant (ϵ_r)	3.5	3.5
Energy width of density of states (σ_E, eV)	0.03	0.03
Exciton diffusion length (L_D, nm)	15	40
Exciton lifetime ($\tau_{exciton}$, s)	1E-8	1E-6
Carrier mobility (μ, $cm^2\ V^{-1}\ s^{-1}$)	7E-4	5E-2
Carrier recombination rate (w_{cr}, s^{-1})	5E5	5E5
Lattice constant (a, nm)	1	1

Table 2: Parameters for the P3HT and PCBM blended films

Property	P3HT	PCBM	Ref
Relative dielectric constant (ϵ_r)	3.9	3.0	[14]
Energy width of density of states (σ_E, eV)	0.063	0.063	[15]
Exciton diffusion length (L_D, nm)	21	5	[16]
Exciton lifetime ($\tau_{exciton}$, s)	6E-10	1.25E-9	[16]
Carrier mobility (μ, $cm^2\ V^{-1}\ s^{-1}$)	2E-4	3E-3	[9]
Carrier recombination rate (w_{cr}, s^{-1})	6E5	6E5	[17]
Lattice constant (a, nm)	1.61	1.61	[18]

Results

Morphology

We studied three different classes of morphologies for the active layer: the bilayer, a chessboard pattern, and the bulk heterojunction. The bilayer is a simple two layer system with a solid layer of acceptor and a solid layer of donor. The chessboard morphology is a pattern of alternating columns of donor and acceptor material. These two morphologies can be seen in Figure 5.

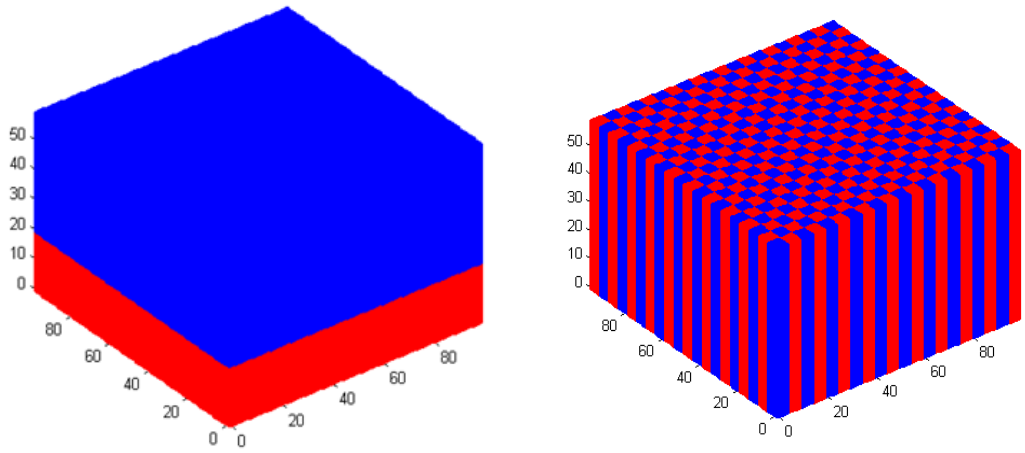

Figure 5: The bilayer[left] and chessboard[right. Red is for donor material and blue is for acceptor material.

The other category of morphology is the bulk heterojunction or BHJ. This morphology is a mixture of acceptor and donor material. BHJ morphologies can be compared by looking at their respective characteristic feature size which is three times the total blend volume divided by the interfacial area [19]. The different morphologies are generated using the previously discussed method. For this initial study, three different BHJ morphologies are used. These were all generated using T = 1 with differing number of Monte Carlo steps. The characteristic feature size calculation is done with the lattice constant of 1 nm for CuPc:C60. To convert to the P3HT:PCBM system, the given characteristic feature size should be multiplied by 1.61 nm, the lattice constant for P3HT and PCBM blend films. The three BHJ morphologies can be seen in Figure 7, and the number of Monte Carlo steps and characteristic feature size for each is shown in Table 3. It is clearly evident from the figures that the films become more ordered and the solid domains of material become bigger as number of Monte Carlo steps increases.

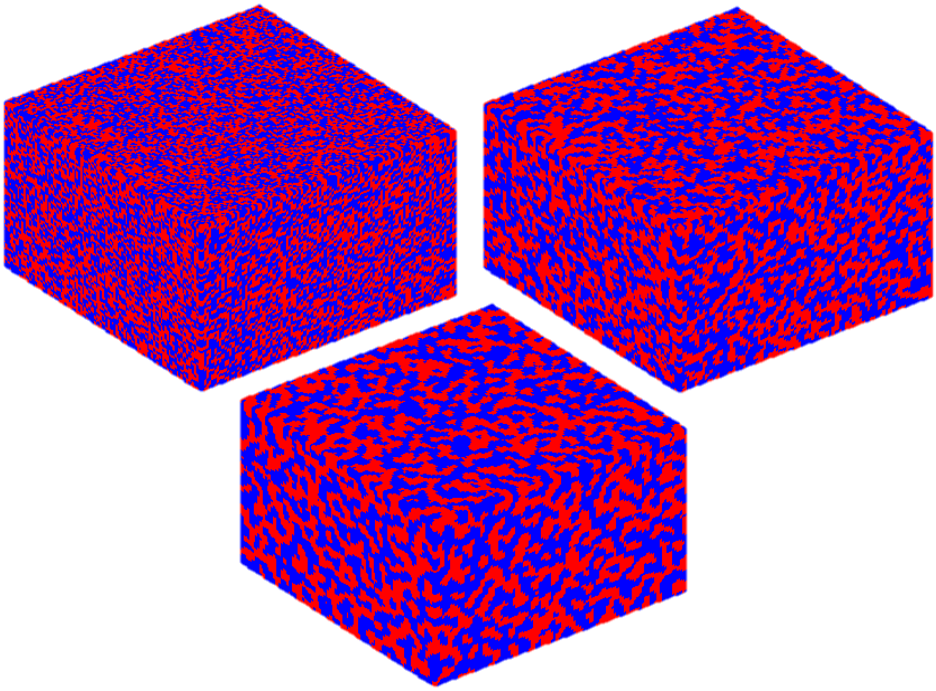

Figure 7: The three BHJ morphologies used in charge transport: 0 MC steps[Left], 10 MC steps [Right], 100 MC steps[Bottom]

Table 3: Parameters for the Generated BHJ Morphologies

Number of Monte Carlo Steps	Characteristic Feature Size (nm)
0	2.02
10	3.46
100	4.54

The temperature dependence on the generated morphology is also examined. Two one hundred Monte Carlo step morphologies were generated. One was generated for T= 1 and the other was generated for T=10. The results can be seen in Figure 6.

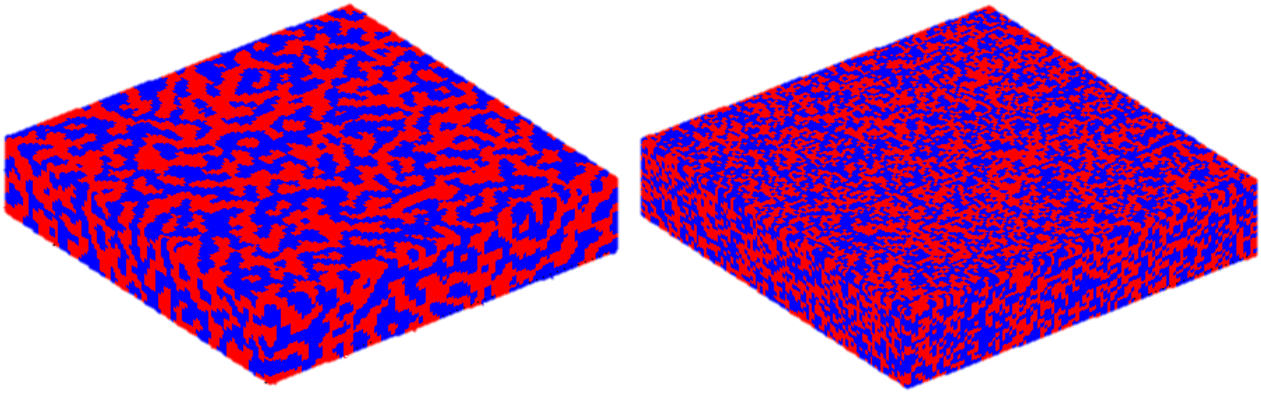

Figure 6: Examining temperature effects on generated morphology. T = 1[Left], T=10[Right]

The effects of raising the temperature leads to lowered characteristic feature sizes. The BHJ on the left has a feature size of 4.6 while the right one has a feature size of 2.2, which is on par with the zero Monte Carlo step BHJ. The higher temperature makes it more likely that a swap which does not lower the energy of the system is accepted.

These results can be used to speed up morphology generation. The time to generate these morphologies using the morphology generator tool built and presented here took a nontrivial amount of time with 100 Monte Carlo steps taking two hours. For future tests, BHJ morphologies with larger characteristic domain sizes may be needed and the time to generate these morphologies may be in the tens of hours. However, by running the tool at different input temperatures this process may be accelerated.

In Figure 8, two 300 MC step BHJ morphologies are shown. The one on the left is a 300 MC step morphology generated at T = 1. The one on the right is a 300 MC step morphology generated by 100 MC steps at T = 1, then 100 MC steps at T = 2, and then 100 MC steps at T = 1. The feature size for the left is 5.07 and the feature size for the right one is 5.7.

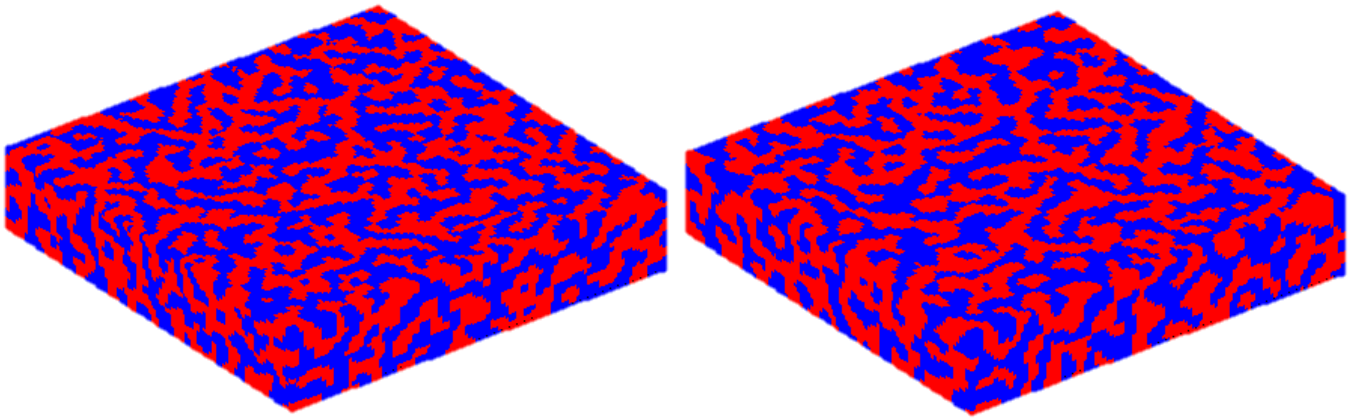

Figure 8: Process to speed up morphology generation. 300 MC, T = 1[Left]; 100 MC, T=1>100 MC T = 2 > 100 MC T = 1[Right]

Exciton Generation Rate

The first cell structure for which the exciton generation rate is calculated is the CuPc:C60 bilayer. Referring back to Figure 4 which defined our solar cell stack from left to right, our structure from left to right is glass substrate, 100 nm ITO, 30 nm PEDOT-PSS, 20 nm CuPc, 40 nm C60, 100 nm aluminum, and then air. The light is considered coming from the left and incident on the glass substrate. The optical field in the CuPc:C60 active layer is calculated as a function of both wavelength and distance from the reflective aluminum cathode. Since the optical field is a function of distance from the reflective aluminum cathode, the z-axis starts at the aluminum cathode so the

active layer is from -60 nm to 0 nm. The optical field is multiplied with the absorption coefficient and the result is integrated over the wavelengths from 300 nm to 900 nm. The result is shown in Figure 9. The discontinuity in the plot can be understood by remembering that it is the electric displacement field (D-field) that is continuous across changes in material, but the electric field is discontinuous due to the change in permittivity. The overall exciton generation rate of 4.08E7 excitons/second for this structure can be found by integrating over Figure 9. The absorption efficiency is 0.7464. The distribution of excitons in this cell will match the shape of the curve in Figure 9. This is the exciton generation rate and distribution used for the CuPc:C60 bilayer morphology charge transport simulation.

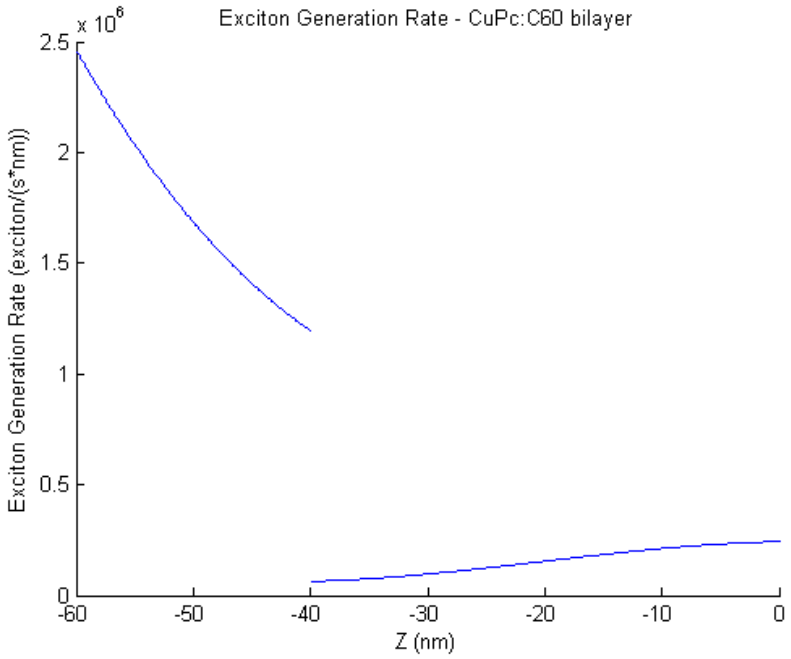

Figure 9: Exciton Generation Rate for a CuPc:C60 bilayer

The next cell structure is the CuPC:C60 bulk heterojunction blend. The structure of the cell from left to right is a glass, 100 nm ITO, 30 nm PEDOT-PSS, 60 nm BHJ blend of CuPc and C60, 100 nm aluminum, and then air. The previous calculations were repeated with this new structure and Figure 11 is the resulting plot. There are no discontinuities since the blend was treated as having a single index of refraction. The exciton generation rate for the CuPc:C60 blend is 5.12E7 excitons/second. The absorption efficiency is 0.8133. This excition generation rate and distribution is used for the chessboard and all of the BHJ morphologies.

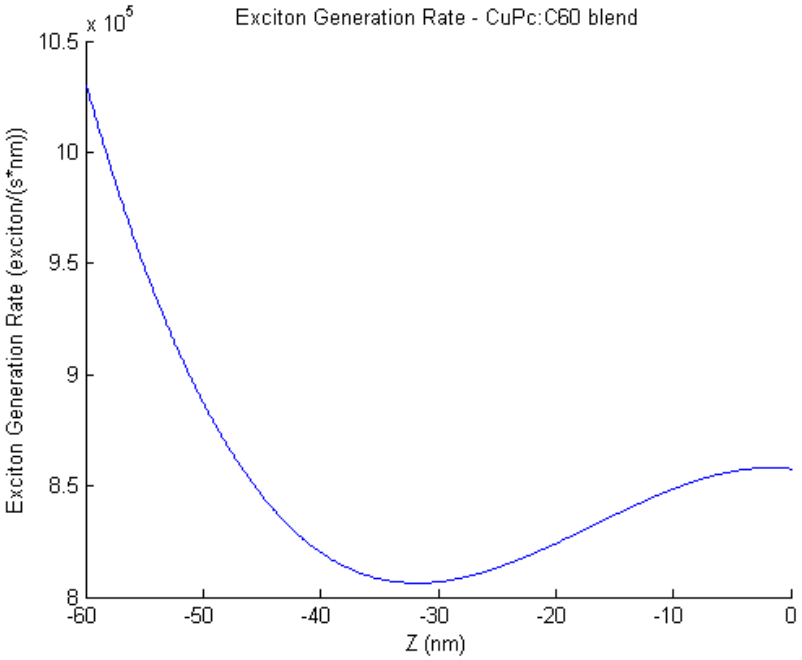

Figure 11: Exciton Generation CuPc:C60 blend

The last structure is for a blend of P3HT:PCBM. The structure is the same as the blend for the CuPc:C60 with the only difference being the active layer materials. The resulting excition generation rate plot is showing in Figure 10. The overall exciton generation rate for this structure is 2.22E7 excitons/second. The absorption efficiency is 0.7023. This exciton generation rate and distribution is used for the P3HT: PCBM chessboard and BHJ morphologies.

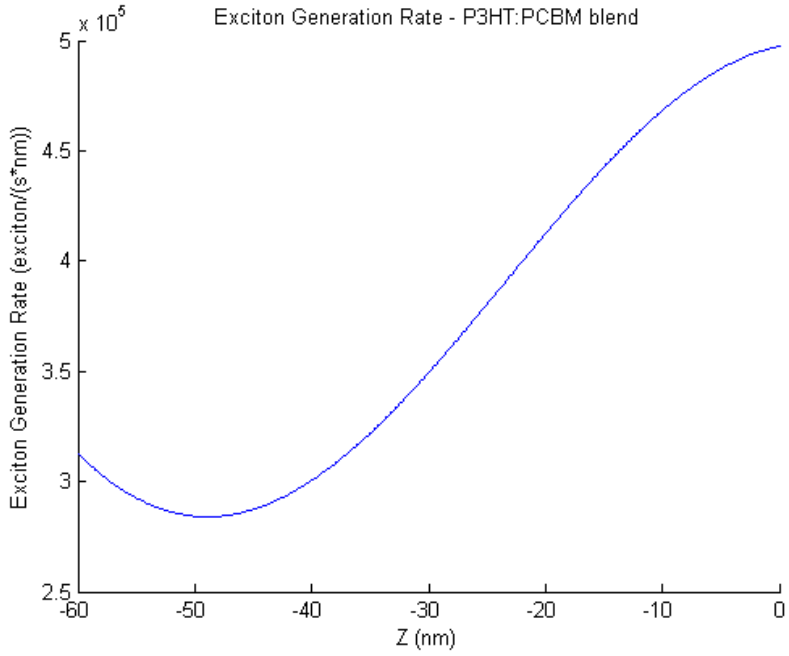

Figure 10: Exciton Generation Rate for P3HT:PCBM

Charge Transport Model

For every morphology and material system, the charge transport model was run for at least 10 μs. Since the dynamics within the system are on the scale of nanoseconds and picoseconds, 10 μs is enough time for the system to reach a steady state. The efficiencies were calculated at steady state. Steady state is when the rate of exciton dissociation equals the rate of charge carrier collection plus the rate of charge carrier recombination. This can be determined by examining how the number of charge carriers in the system changes: at steady state the charge carrier number should be approximately constant.

Four numbers are tracked as the charge transport model runs: number of carriers in the cell, total number of holes collected, total number of electrons collected, total number of excitons created, and total number of excitons dissociated. Once steady state is achieved, the efficiencies are determined. For the exciton dissociation efficiency η_{ED}, it is the number of excitons dissociated over some large time period divided by number of excitons generated over that same large time period. For charge collection η_{CC}, it is the number of collected holes plus the number of collected electrons over some large time period divided by the two times the number of dissociated excitons over that same large time period. The results of the simulation for the two material systems are shown in Table 4 and Table 5.

Table 4: Efficiency of CuPc and C60 films

Morphology	η_{ED}	η_{CC}	η_{IQE}	η_{α}	η_{EQE}
Bilayer	.7448	1	.7448	0.7464	0.5559
Chessboard	1	0.9974	0.9974	0.8133	0.8112
0 MC steps	1	0.9967	0.9967	0.8133	0.8106
10 MC steps	1	0.9919	0.9919	0.8133	0.8067
100 MC steps	1	0.9982	0.9982	0.8133	0.8118

Table 5: Efficiency of P3HT and PCBM films

Morphology	η_{ED}	η_{CC}	η_{IQE}	η_{α}	η_{EQE}
Chessboard	.9142	.9859	.9013	0.7023	0.6330
0 MC steps	1	.9158	.9158	0.7023	0.6432
10 MC steps	.9145	.9901	.9054	0.7023	0.6359
100 MC steps	.9957	.9601	.9560	0.7023	0.6714

The average number of charge carriers in the cell is directly related to the carrier collection efficiency. The larger the average number of carriers is, the smaller the efficiency will be. For the CuPc:C60 material system, the average number of charge carriers was 0.93 for the bilayer and up to 7.63 for the 0 MC step BHJ. This is compared to the lowest average of 25.32 for the chessboard of P3HT:PCBM. Accordingly, the efficiencies for the CuPc:C60 morphologies are higher than their P3HT:PCBM counter parts.

Largely, the values obtained make sense. The perfect exciton diffusion efficiencies make sense for CuPc:C60 because the exciton diffusion length is 15 nm and 40 nm for CuPc and C60 respectively. The chessboard morphology's columns are only 5 nm by 5 nm and the BHJ morphologies all had feature sizes less than 5 nm. Perfect dissociation efficiency makes sense. The bilayer's high dissociation efficiency is also understandable because the CuPc and C60 layers are 20 nm and 40 nm thick respectively, very close to the diffusion length for those materials. The only slightly troubling item is that the charge collection efficiency is higher for 0 MC step BHJ compared to 10 MC step BHJ contrary to theory. However, the difference is so minute and their average carrier number so close (7.63 compared to 6.23) that this result could be an artifact from the efficiency calculation.

For the P3HT and PCBM morphology, everything is consistent with predicted trends except for 100 MC steps. The values for 100 MC steps are out of step with every trend. Large feature sizes should result in lower exciton dissociation and higher charge collection but the opposite is observed for the 100 MC step morphology.

Discussion

The results from the CuPc:C60 tests generally do not match the corresponding results from the work done by Yang and Forrest. They simulated a η_{ED} of 0.25 for the 60 nm bilayer compared to the value of 0.7448 presented here. For BHJ morphologies with similar characteristic feature sizes, they had η_{CC} = 0.34 compared to the near unity values obtained here. Several possible reasons for these discrepancies are discussed here.

Yang and Forrest did not account for a PEDOT-PSS layer when computing the exciton generation rate and distribution. They also did not state how thick their ITO layer was assumed to be, and also they used a silver contact of unknown thickness compared to the aluminum contact used here. Furthermore, the indices of refractions for these materials can vary a fair amount depending on how they are deposited, and it is unknown exactly what numbers Yang and Forrest

used for their calculation. Also to be considered are the many edge cases in the charge transport simulation that were not fully explained such as what happens when a hole tries to recombine with an electron, but the electron is no longer there.

However, the largest difference from Yang and Forrest's work is the exciton hopping time. The version used in this work can be seen in Equation 29. The key is that the exciton localization radius R_0 was fitted so that the excition should diffuse the correct amount given its lifetime. Yang and Forrest used the following:

$$\tau_{eh} = -\tau_{ex}\left(\frac{R_{ij}}{L_d}\right)^6 \frac{\ln(X)}{f(\Delta E_{ij})} \tag{32}$$

where L_d is the diffusion length of the excition. An excition in CuPc will have a diffusion length of 15 nm. Assuming $-\frac{\ln(X)}{f(\Delta E_{ij})}$ = 1, and R_{ij} = 1 nm (which it generally is), then this exciton will have a hop time of 9E-16 seconds or a hop time of 900 attoseconds. This corresponds to 1.1E7 hops for one exciton lifetime. If the exciton moves like a particle undergoing a random walk, then it will travel the square root of 1.1E7 nm for a distance of 3375 nm which is significantly larger than its diffusion length of 15 nm. In fact, using this equation should give Yang and Forrest perfect excition dissociation for every morphology. They did not report perfect dissociation so it seems there is a mistake somewhere.

The performance for the P3HT:PCBM makes more sense. From the literature, internal quantum efficiencies of 0.8 have been reported [20] [21]. The simulated IQE of 0.9 presented here is not that different from these experimental values. Also, the parameters for P3HT:PCBM films can vary greatly depending on how they are constructed or measured. For example 21 nm was the exciton diffusion length used for P3HT in the simulation; however some researchers have reported diffusion lengths as low as 3 nm [22] . This could greatly change the final simulation values.

Conclusions and Future Work

A Dynamical Monte Carlo simulation has been developed to simulate organic solar cell performance. Besides just the charge transport simulation model, all accompanying tools needed to simulate a variety of organic solar cells have also been constructed. These tools include code to calculate exciton generation rate and distribution, generate random bulk heterojunction morphologies, classify those bulk heterojunction morphologies according to characteristic feature size, and generate figures of those BHJ morphologies. Even though everything was originally

designed to be used with the CuPc:C60 material system, it was a simple procedure to convert to the P3HT:PCBM system and generate results close to experimental values.

Future work be will focused on further testing of the P3HT:PCBM material system such as simulations of BHJ morphologies with bigger domain sizes, changing the input parameters, more trials of current morphologies, etc. Eventually the goal will be experimental confirmation of the simulation results and eventual usage of the simulation to help guide solar cell design.

Acknowledgements

I would like to thank Prof Adrienne D. Stiff-Roberts for her immense amount of patience as she guided me on this work. I also thank Prof. Ian Dinwoodie for talking to me about Monte Carlo simulations, Prof. Robert Brown for explaining some issues I had with computer based Monte Carlo simulations, and Prof Stephen Teitsworth for helpful conversations. I would also like to thank Ryan McCormick for always being there to listen and offer advice whenever I hit a roadblock. Lastly, I would like to thank Dean Martha Absher for the opportunity offered by her Pratt Fellows Program.

Works Cited

[1] C. W. Tang, "Two-Layered Organic Photovoltaic Cell," *Appl. Phys. Lett.,* vol. 48, pp. 183-185, 1986.

[2] M. A. Green, K. Emery, Y. Hishikawa, W. Warta and E. D. Dunlop, ""Solar cell efficiency tables (version 39)"," *Progress in Photovoltaics: Research and Applications,,* vol. 20, pp. 12-20, 29 February 2012.

[3] L. Li, "Dissertation: Charge Transport in Organic Semiconductor Materials and Devices," Vienna University of Technology, Vienna, 2007.

[4] P. Peumans, A. Yakimov and S. R. Forrest, "Small Molecular Weight Organic Thin-Film Photodetectors and Solar Cells," *J. Appl. Phys.,* vol. 93, pp. 3693-3723, 2003.

[5] P. K. Watkins, A. B. Walker and G. L. Verschoor, "Dynamical Monte Carlo Modelling of Organic Solar Cells: The Dependence of Internal Quantum Efficiency on Morphology," *Nano Letters,* vol. 5, no. 9, pp. 1814-1818, 2005.

[6] F. Yang and S. R. Forrest, "Photocurrent Generation in Nanostructured Organic Solar Cells," *ACS*

Nano, vol. 2, no. 5, pp. 1022-1032, 2008.

[7] P. Peumans, Y. Aharon and F. R. Stephen, "Erratum: "Small molecular weight organic thin-film photodetectors and solar cells" [J. Appl. Phys. 93, 3693 (2003)]," *J. Appl. Phys.,* vol. 95, no. 5, p. 2938, 2004.

[8] D. Datta, V. Tripathi, P. Gogoi, S. Banerjee and S. Kumar, "Ellipsometric studies on thin film CuPC:C60 blends for solar cell applications," *Thin Solid Films,* vol. 516, pp. 7237-7240, 2008.

[9] F. Monestier, J. Simon, P. Torchio, L. Escoubas, F. Flory, S. Bailly, R. de Bettignies, S. Guillerez and C. Defranoux, "Modeling the short-circuit current density of polymer solar cells based on P3HT:PCBM blend," *Sol. Energy Mater. Sol Cells,* 2006.

[10] H. Hoppe, N. S. Sariciftci and D. Meissner, "Optical Constants of Conjugate Polymer/Fullerene Based Bulk-Heterojunction Organic Solar Cells," *Mol. Cryst. Liq. Cryst.,* vol. 385, pp. 233-239, 2002.

[11] M. Polyanskiy, "Refractive Index Database," 2012. [Online]. Available: http://refractiveindex.info/. [Accessed 19 March 2012].

[12] H. Bassler, "Charge transport in disordered organic photoconductors," *Phys. Stat. Sol.(b),* vol. 175, pp. 15-55, 1993.

[13] A. Miller and E. Abrahams, "Impurity Conduction at Low Concentrations," *Physical Review,* vol. 120, no. 3, pp. 745-755, 1960.

[14] J. Szmytkowski, "Modeling the electrical characteristics of P3HT:PCBM bulk heterojunction solar cells: Implementing the interface recombination," *Semicond. Sci. Technol,* vol. 25, 2010.

[15] P. P. Boix, G. Garcia-Belmonte, U. Munecas, M. Neophytou, C. Waldauf and R. Pacios, "Determination of gap defect states in organic bulk heterojunction solar cells from capacitance measurements," *Appl. Phys. Lett,* vol. 95, 2009.

[16] V. S. Gevaerts, L. Jan Anton Koster, M. M. Wienk and R. A. Jansen, "Discriminating between Bilayer and Bulk Heterojunction Polymer:Fullerene Solar Cells Using the External Quantum Efficiency," *ACS Appl. Mater. Interfaces,* vol. 3, pp. 3252-3255, 2011.

[17] K. S. Nalwa, H. K. Kodali, B. Ganapathysubramanian and S. Chaudhary, "Dependence of recombination mechanisms and strength on processing conditions in polymer solar cells,"

Appl. Phys. Lett., vol. 99, 2011.

[18] T. Erb, U. Zhokhavets, G. Gobsch, S. Raleva, B. Stuhn, P. Schilinsky, C. Waldauf and C. J. Brabec, "Correlation Between Structural and Optical Properties of Composite Polymer/Fullerne Films for Organic Solar Cells," *Adv. Funct. Mater.,* vol. 15, pp. 1193-1196, 2005.

[19] R. A. Marsh, C. Groves and N. C. Greenham, "A microscopic model for the behavior of nanostructured organic photovoltaic devices," *J. Appl. Phys.,* vol. 101, 2007.

[20] J. Jo, S. Na, S. Kim, T. Lee, Y. Chung, S. Kang, D. Vak and D. Kim, "Three-Dimensional Bulk Heterojunction Morphology for Achieving High Internal Quantum Efficiency in Polymer Solar Cells," *Adv. Func. Mater.,* vol. 19, pp. 2398-2406, 2009.

[21] G. F. Burkhard, E. T. Hoke and M. D. McGehee, "Accounting for Interference, Scattering, and Electrode Absorption to Make Accurate Internal Quantum Efficiency Measurements in Organic and Other Thin Solar Cells," *Adv. Mater.,* vol. 22, pp. 3293-3297, 2010.

[22] P. E. Shaw, A. Ruseckas and I. D. Samuel, "Excition Diffusion Measurments in Poly(3-hexylthiophene)," *Adv. Mater.,* vol. 20, no. 18, pp. 3516-3520, 2008.

[23] M. Pope, Electronic Processes in Organic Crystals and Polymers, Oxford University Press, 1999.

[24] S. E. Shaheen, N. Kopidakis, D. S. Ginley, M. S. White and D. C. Olson, "Inverted bulk-heterojunction plastic solar cells," SPIE Newsroom, 24 May 2007. [Online]. Available: http://spie.org/x14269.xml. [Accessed 14 April 2012].

[25] V. Sundström and C. S. J. Ponseca, "Transport in organic solar-cell materials studied by time-resolved terahertz spectroscopy," Lund University, 29 October 2007. [Online]. Available: http://www.chemphys.lu.se/research/projects/teratransport/. [Accessed 14 April 2012].